Supplementary Information

Simultaneous whole-animal 3D-imaging of neuronal activity using light field microscopy

Robert Prevedel[1-3,10], Young-Gyu Yoon[4,5,10], Maximilian Hoffmann[1-3], Nikita Pak[5,6], Gordon Wetzstein[5], Saul Kato[1], Tina Schrödel[1], Ramesh Raskar[5], Manuel Zimmer[1], Edward S. Boyden[5,7-9] and Alipasha Vaziri[1-3]

[1]Research Institute of Molecular Pathology, Vienna, Austria.
[2]Max F. Perutz Laboratories, University of Vienna, Vienna, Austria.
[3]Research Platform Quantum Phenomena & Nanoscale Biological Systems (QuNaBioS), University of Vienna, Vienna, Austria.
[4]Department of Electrical Engineering and Computer Science, Massachusetts Institute of Technology (MIT), Cambridge, MA, USA
[5]MIT Media Lab, Massachusetts Institute of Technology (MIT), Cambridge, MA, USA
[6]Department of Mechanical Engineering, Massachusetts Institute of Technology (MIT), Cambridge, MA, USA
[7]Department of Biological Engineering, Massachusetts Institute of Technology (MIT), Cambridge, MA, USA
[8] Department of Brain and Cognitive Sciences, Massachusetts Institute of Technology (MIT), Cambridge, MA, USA
[9] McGovern Institute, Massachusetts Institute of Technology (MIT), Cambridge, MA, USA

[10] These authors contributed equally to this work.

Correspondence should be addressed to E.S.B. (esb@media.mit.edu) or A.V. (vaziri@imp.ac.at).

Supplementary Figures

Supplementary Figure 1. Whole-animal Ca^{2+}-imaging of *C. elegans*.

Supplementary Figure 2. High-resolution images of Fig. 2e and Fig. 2f indicating Neuron ID numbers in z-planes and heatplot map of neuronal activity of all neurons.

Supplementary Figure 3. Identification of neuron classes in *C. elegans* during chemosensory stimulation.

Supplementary Figure 4. High-speed Ca^{2+}-imaging of unrestrained *C. elegans*.

Supplementary Note 1 General principle, optical design choices and their effect on resolution in 3D deconvolution light field microscopy.

Supplementary Note 2 Volume reconstruction for 3D-deconvolution light field microscopy and computing requirements.

Supplementary References

Supplementary Figure 1. Whole-animal Ca^{2+}-imaging of *C. elegans*.

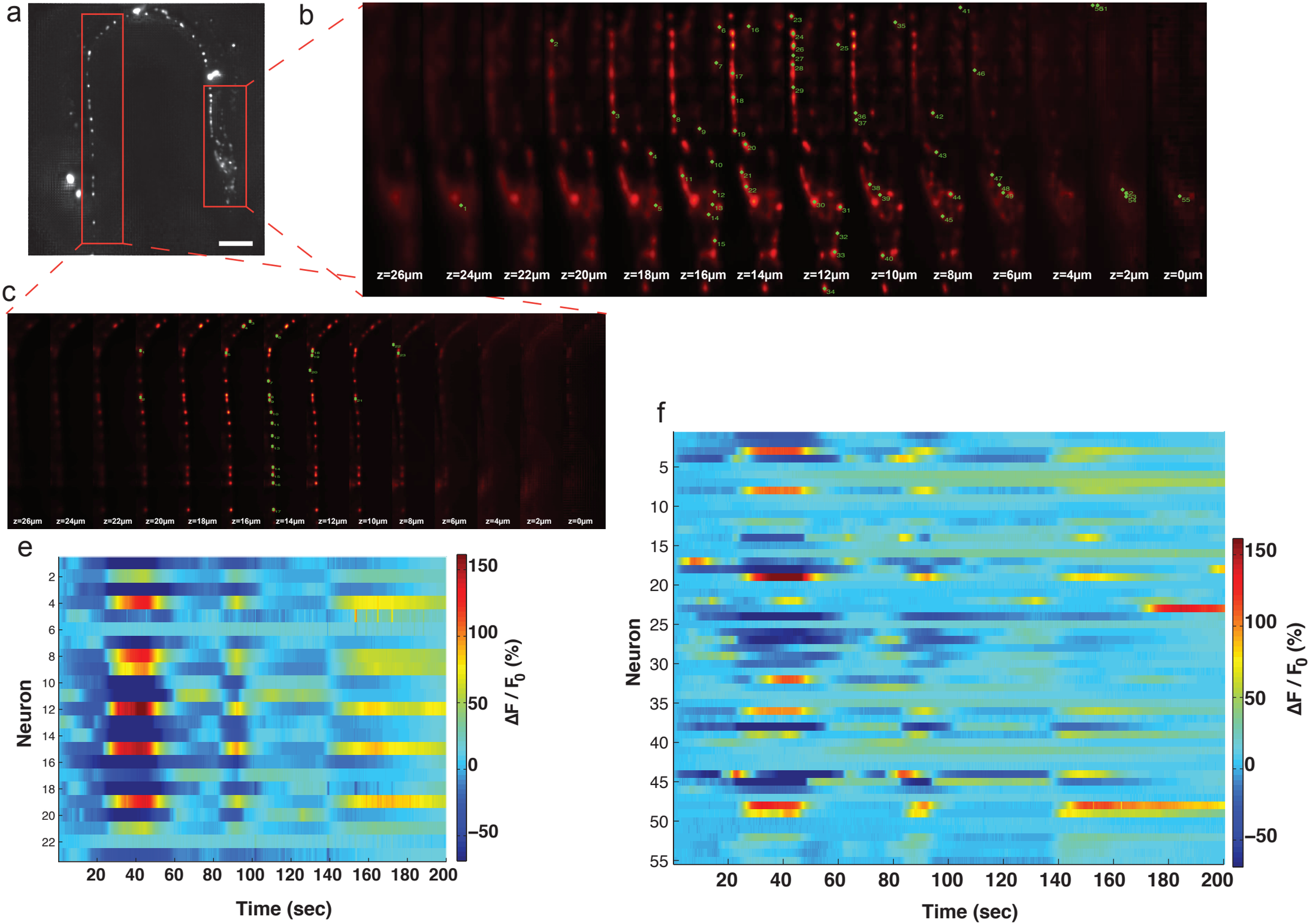

Supplementary Figure 1. Whole-animal Ca^{2+}-imaging of *C. elegans*.
(**a**) Maximum intensity projection (MIP) of light field deconvolved image (15 iterations) of the whole worm shown in Fig. 2d, containing 14 distinct *z*- planes. Neurons contained in red boxes were further analyzed in (**b-f**). NeuronIDs of *z*-stack in **b** match with heatmap plot of neuronal activity in **f** and show neurons identified in the head using an automated segmentation algorithm, while **c** shows neuronIDs along the ventral cord with corresponding heatplot map shown in **e**. Scale bar 50 μm.

Supplementary Figure 2. High-resolution images of Fig. 2e and Fig. 2f indicating Neuron ID numbers.

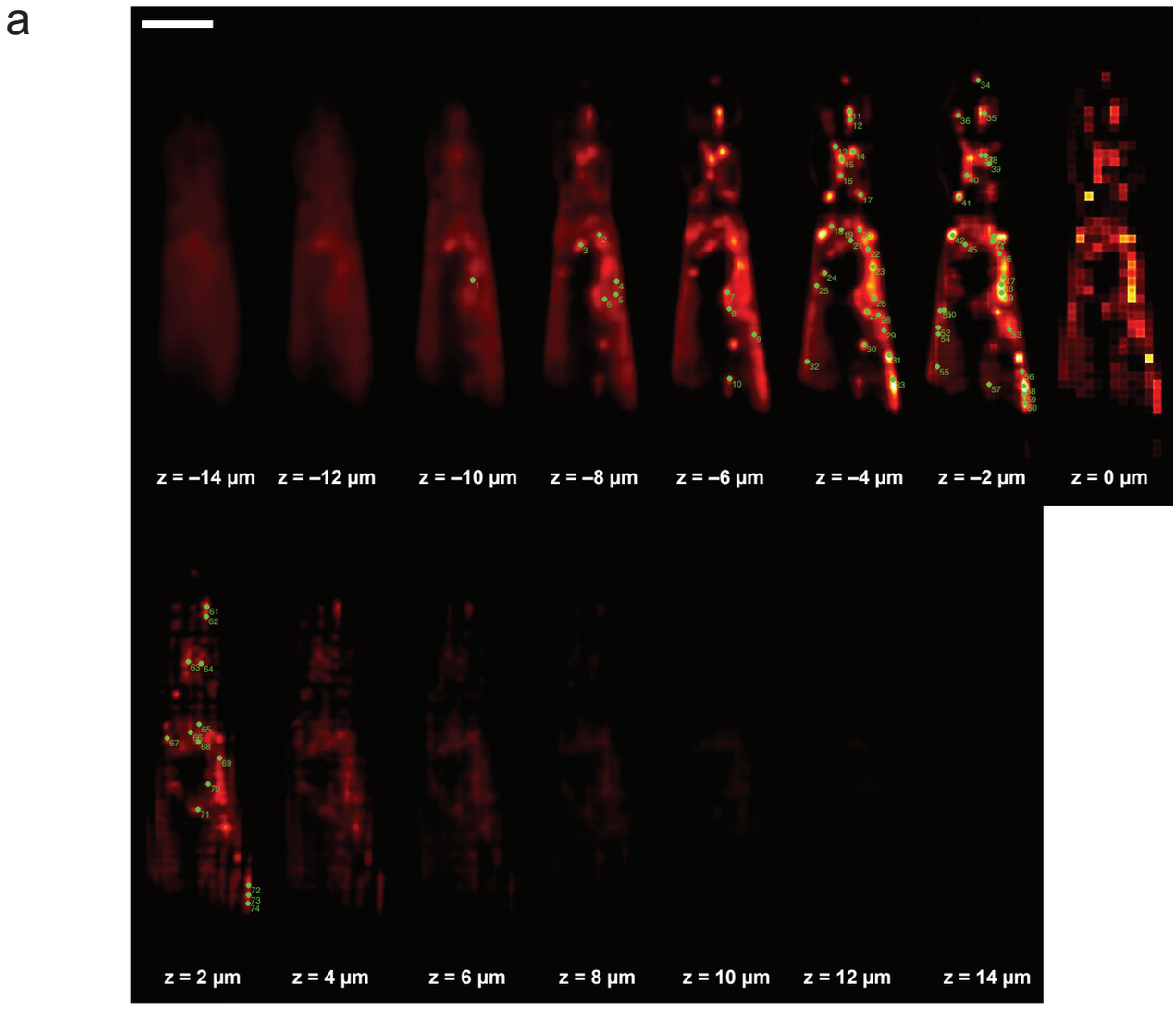

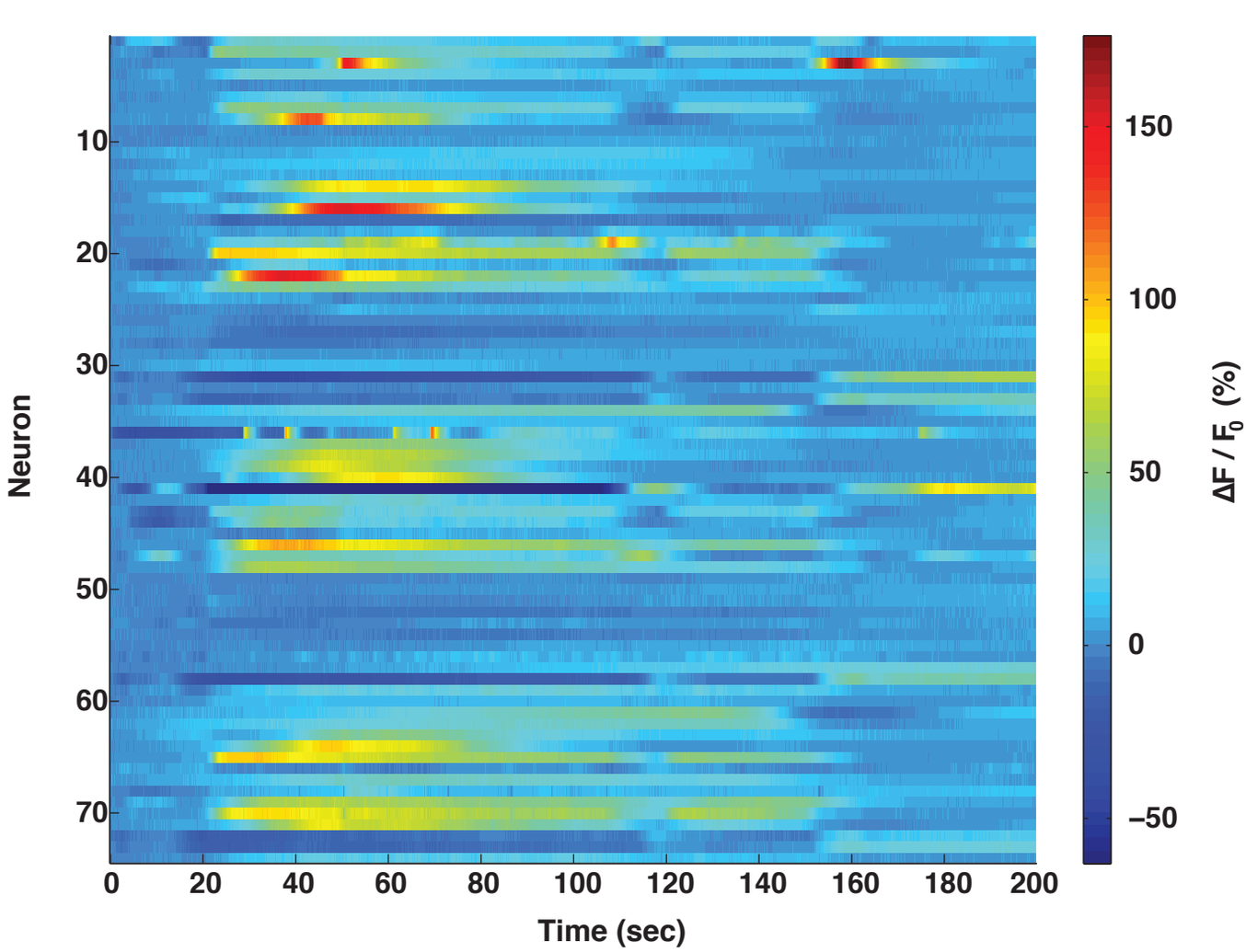

Supplementary Figure 2. High-resolution images of Fig. 2e and Fig. 2f indicating Neuron ID numbers in *z*-planes in (**a**) and heatmap plot of neuronal activity of all neurons in (**b**).

Supplementary Figure 3. Identification of neuron classes in *C. elegans* during chemosensory stimulation.

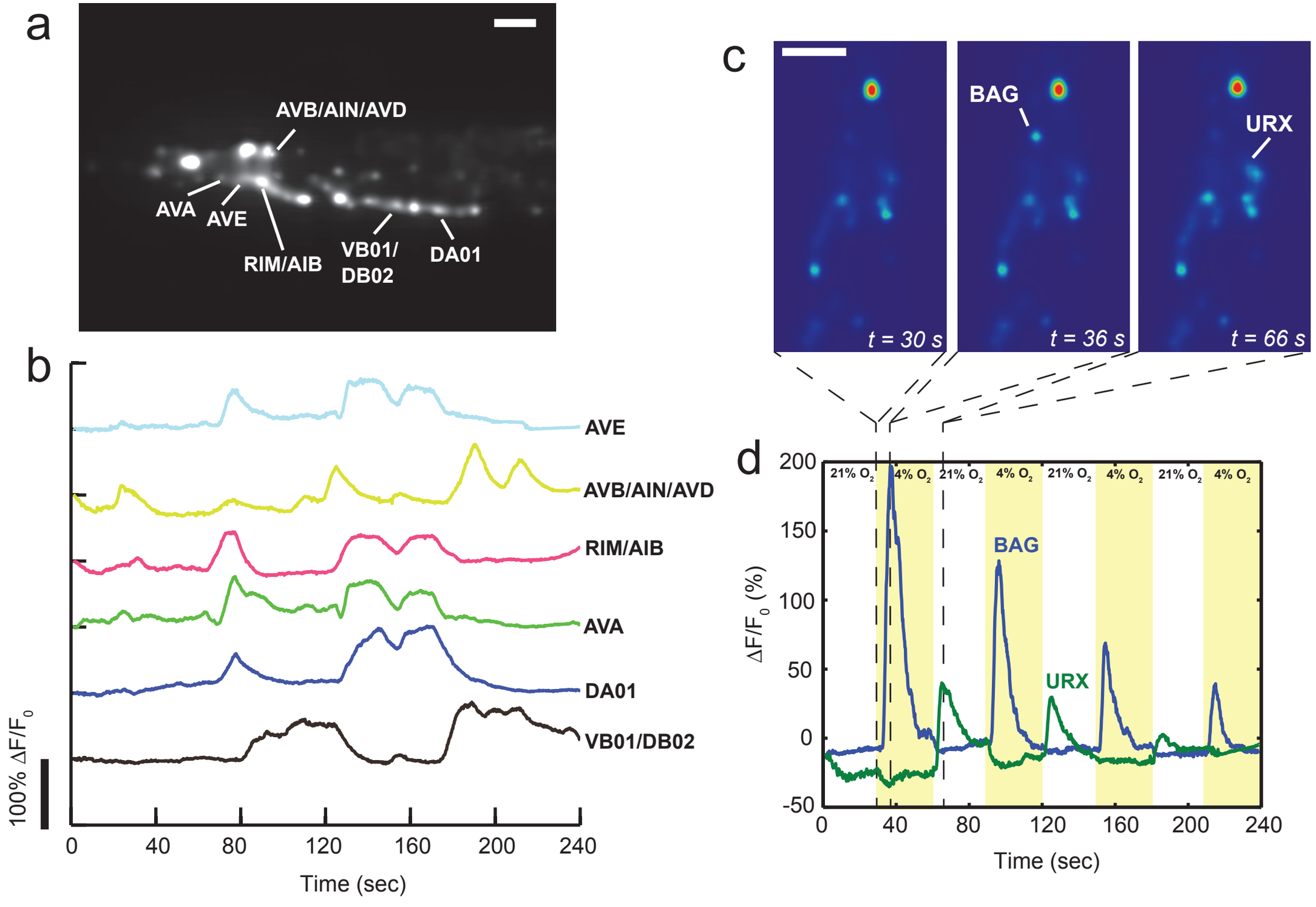

Supplementary Figure 3. Identification of neuron classes in *C. elegans* during chemosensory stimulation.
Whole brain LFDM recording at 5 Hz of *C. elegans* under consecutively changing O_2 concentrations (30 seconds time-shifts). (**a**) Maximum intensity projection (MIP) of light field deconvolved image (8 iterations) of the worm's head region, containing 7 distinct *z*-planes. Neuron classes were identified based on location and typical Ca^{2+}-signals, whose individual traces are shown in **b**. (**c**) Individual *z*-plane containing the oxygen-downshift sensing neuron BAG at various time-points before, during and after stimulus, respectively. (**d**) Fluorescence traces of oxygen sensory neurons BAG and URX, with varying O_2 concentrations indicated by shading. Scale bar is 20 μm in **a** and **c**.

Supplementary Figure 4. High-speed Ca^{2+}-imaging of unrestrained *C. elegans* at 50 Hz.

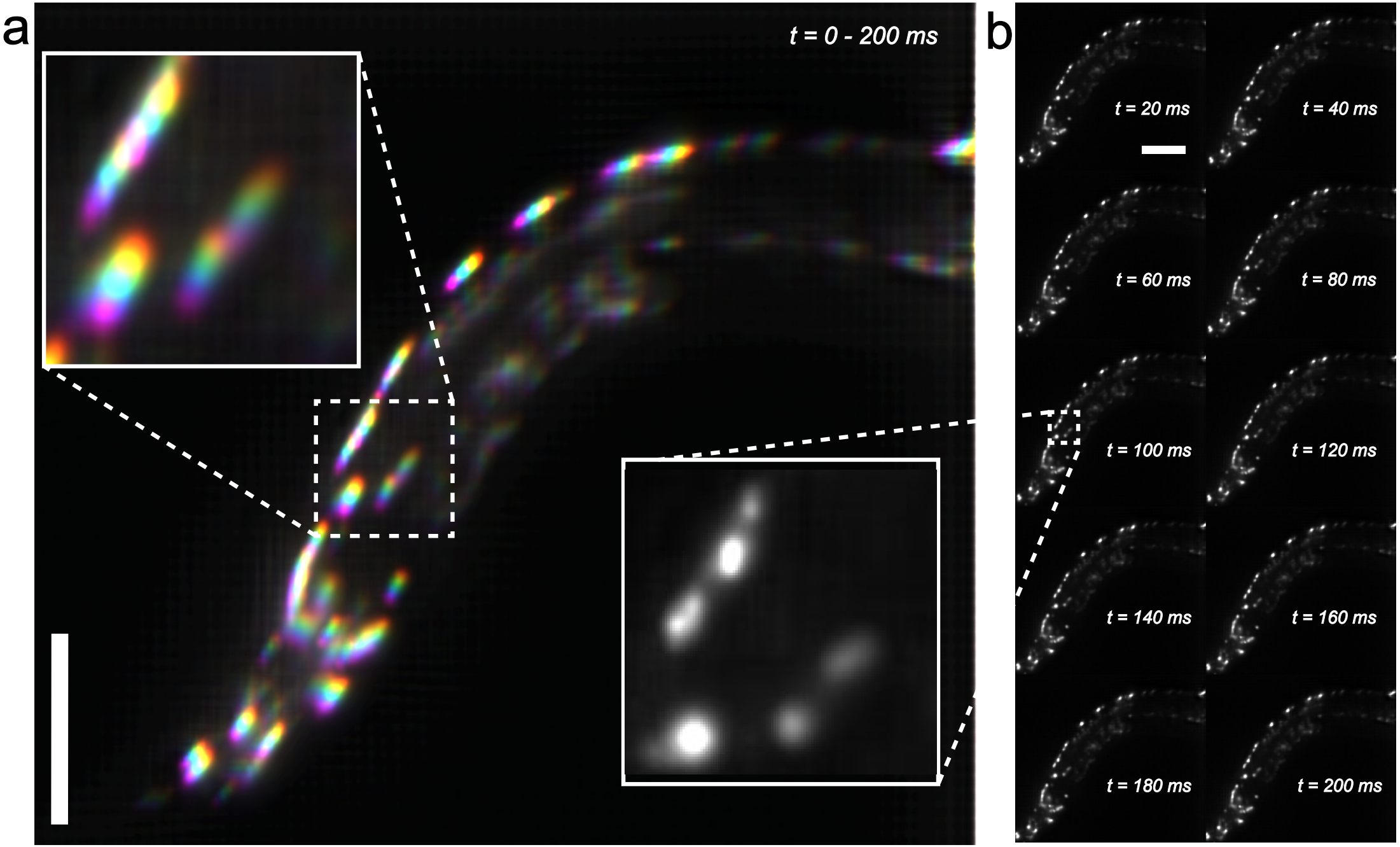

Supplementary Figure 4. High-speed Ca^{2+}-imaging of unrestrained *C. elegans* at 50 Hz. Selected time-series of the LFDM recording of freely-moving worms at 50 Hz shown in **Supplementary Video 4**. (**a**) Overlay of 10 consecutive frames, with colors coding for different time-points. This is equivalent to an effective frame-rate of 5 Hz. At this speed, motion blur would lead to ambiguous discrimination of individual neurons, as is clearly visible in the inset. In contrast, in (**b**) we show the individual frames of the same time-series as recorded with 50 Hz (20 ms exposure time). At this speed, motion blur is almost non-existent. This demonstrates that 50 Hz are sufficient to follow the activity of unrestrained worms, especially if additional worm tracking would be employed. Scale bar is 50 μm in **a** and **b**. Also see **Supplementary Video 3**.

Supplementary Note 1 General principle, optical design choices and their effect on resolution in 3D deconvolution light field microscopy.

Generally speaking, a conventional 2-D microscope captures a high-resolution image of a specimen that is in focus. For volumetric specimens, the same image, however, also contains blurred contributions of areas that are optically out of focus. Unmixing them in post-processing is an ill-posed problem and usually not possible. Scanning microscopes solve this problem by measuring each point in the 3-D volume sequentially. While this is an effective process, it is time-consuming and not always applicable to capturing dynamic events or moving specimens. Light field microscopes change the optical acquisition setup to capture different primitives: instead of recording individual points sequentially, light field microscopes capture "rays" of light, that their summed emission through the 3-D volume. Instead of recording them in sequence, a set of "rays" – the light field **–** is multiplexed into a single 2-D sensor image. This spatial, rather than temporal, approach to multiplexing drastically improves acquisition speed at the cost of reduced resolution. To recover the 3-D volume from measured emission, a computed tomography problem has to be solved. Following Ref. 1, we implement this reconstruction step as a deconvolution. Please note that while the light field is conceptually comprised of geometric rays, in practice the image formation and inversion also considers diffraction, as discussed in the primary text.

Light field microscopes support all objective magnifications, but usually benefit from a high numerical aperture (NA) and microlenses that are matched with the NA of the employed objective. The choice of objective and microlens array determines the spatial resolution and field-of-view in all three dimensions. The pitch, i.e. the distance between the microlenses, in combination with the sensor's pixel size and objective magnification controls trade-off between spatial resolution vs. field-of-view while the objective's magnification and numerical aperture control axial resolution vs. axial range. Furthermore, the field-number of the microlenses needs to match that of the objective in order to preserve the maximum angular information in the light fields [2].

Due to the variation in sampling density, reconstructed volumes have a lateral resolution that varies along the optical axis. On the focal plane, achievable resolution is equivalent to conventional LFM, i.e. the size of each microlens divided by the magnification of the objective lens (150 μm / 40x = 3.75 μm in our system). The resolution increases for lateral sections close to the focal plane, ~1.5µm laterally in our implementation, but drops at larger distances, e.g. to ~3 μm laterally at -25 μm, in accordance with Ref. [1]. We find similar behavior with the 20x 0.5NA lens used in our zebrafish recordings. Here we find a maximum resolution of ~3.4 μm (~11 μm) laterally (axially) based on a reconstructed point spread function (see also **Fig. 3a**).

It is also possible and straightforward to design microlens arrays for higher magnification objectives in order to look at smaller samples. Following the criteria outlined in Ref. 2, microlenses can be designed taking into account the trade-offs between lateral and axial resolution. For instance we have performed simulations for a 100x 1.4NA oil objective and a f-number matched microlens of 100 μm pitch, and found that our LFDM should have a resolution of ~0.27 μm (1 μm) laterally (axially). The lateral field of view would be 140 μm with a sCMOS camera similar to the one used in this work and we would expect a useful axial range of 10-15 μm.

Supplementary Note 2 Volume reconstruction for 3D-deconvolution light field microscopy and computing requirements.

The software for 3D reconstruction was written in MATLAB (Mathworks) using its parallel computing toolbox to enable multi-core processing, and allows choosing between CPU- and GPU-based executions of the algorithm. The software consists of three different parts: point spread function (PSF) computation, image rectification / calibration, and 3D volume reconstruction. To generate PSFs, we compute the wavefront imaged through the microlens array for multiple points in the volume using scalar diffraction theory [3]. We also exploit the circular symmetry of PSF for its computation, which results in a boost in computational speed. To faithfully represent the high spatial frequency component of the wavefront, computations are performed with a spatial oversampling factor of 3x compared to the size of the virtual pixels that correspond to the resampled image.

For the image rectification and calibration, the size and location of each microlens with respect to the sensor pixels are estimated using calibration images showing a fluorescent slide and a collimated beam. An open source software named LFDisplay [http://graphics.stanford.edu/software/LFDisplay/], for example, can be used to locate the microlenses with respect to the pixels. Once the size and the location of each microlens is determined, captured images are resampled to contain 15 x 15 (11 x 11) angular light field samples under each microlens. The target axial resolution of reconstructed volumes is 2 (4) μm, which requires 12-16 (51) z-slices for worm (zebrafish) samples.

The essential operations for volume reconstruction are based on computing large number of 2-dimensional convolutions. Therefore reconstruction speed depends heavily on the implementation of the convolution operation and its speed. Using the convolution theorem, this problem can be accelerated by computing on graphical processor units (GPUs) in the Fourier domain. The underlying fast Fourier Transform (FFT) can be computed in $O(n \log n)$ operations whereas conventional convolution requires $O(n^2)$ operations. Furthermore, the FFT is well suited for GPU computing, and we found this to result in significant (up to 20x) reduction in computing time compared to 12-core CPU based execution. With GPU computing method, reconstructing individual frames of recorded image sequences using Richardson-Lucy deconvolution method took between 2 and 6 min, depending on the size of the image, on a workstation with one Nvidia Tesla K40c GPU and 128GB of RAM. Specifically, the reconstruction of only the head ganglia region of *C. elegans* (Fig. 2c-e) took about 2 minutes where the reconstruction of the whole C. elegans took about 6 minutes with 8 iterations of the deconvolution algorithm. Similar times were measured for zebrafish volume reconstructions.

In comparison, CPU based computing on 12 parallel cores required between 5 and 30 min. However, by parallelizing the reconstruction on a medium sized cluster employing ~40 nodes, we found that a typical 1000 frame movie of whole *C.elegans* (such as in **Supplementary Video 1**) could be reconstructed within ~12 hours. Cloud based computing options, e.g. through Amazon Web Services and other competing online tools, might also provide efficient means for large-scale volume reconstruction.

Reconstruction times of image sequences could be further optimized by using the reconstructed volume of one frame as the initial guess for the next. This removes the need for multiple algorithmic iterations at each frame and is well-justified because the imaging speed was sufficiently faster than both neuronal activity and movement of the worm.

Supplementary References

1. Broxton, M. et al., *Optics Express* **21**, 25418 (2013).
2. M. Levoy, M. et al., *ACM Trans. Graph.* **25**, 924 (2006).
3. Gu, M. Advanced Optical Imaging Theory, *Springer* **ISBN-10: 981402130X** (1999).